Hindawi
Shock and Vibration
Volume 2022, Article ID 7494264, 14 pages
https://doi.org/10.1155/2022/7494264

Research Article

Genesis Analysis and Stability Evaluation of Karst Area in the Mudengdong Village Based on the Geological Investigation and Numerical Simulation Methods

Hanhua Xu,[1,2] Kuiming Liu,[3] Wenlian Liu,[1,2] Chun Zhu,[4] Sitao Zhu,[5] and Jiaxiang Dong[6]

[1]*Kunming Prospecting Design Institute of China Nonferrous Metals Industry Co., Ltd, Kunming 650051, Yunnan, China*
[2]*Yunnan Key Laboratory of Geotechnical Engineering and Geohazards, Kunming 650051, Yunnan, China*
[3]*State Key Laboratory for Geomechanics & Deep Underground Engineering, China University of Mining & Technology (Beijing), Beijing 100083, China*
[4]*School of Earth Sciences and Engineering, Hohai University, Nanjing 210098, China*
[5]*School of Civil and Resource Engineering, University of Science and Technology Beijing, Beijing 100083, China*
[6]*Faculty of Electric Power Engineering, Kunming University of Science and Technology, Kunming 650500, Yunnan, China*

Correspondence should be addressed to Kuiming Liu; liukm1996@126.com

Received 11 April 2022; Revised 9 May 2022; Accepted 2 June 2022; Published 6 July 2022

Academic Editor: Pengfei Wang

The large-scale mining of underground mineral resources will lead to the formation of mined-out areas, which will lead to a series of geological and environmental problems. By selecting the Mudengdong village as a case study, this paper uses geodetic satellite remote sensing technologies to perform qualitative analyses and summarize the geological engineering conditions of the factory. Afterwards, the predominant factors that affect the stability of foundation are determined based on the geological survey of karst in goaf structures. Finally, the finite element software ANSYS is used to comprehensively study the karst problem. The results indicate that (1) the karst development pattern in the study area is controlled by the Beiyin mountain fault, in which case the karst in the basin, in the foot slope, or in the pass section is more widespread than in the slope section. Moreover, the karst generally has a vertical form and is in the early karst stage of development; (2) surface rainwater infiltration, earthquakes, and load pressure are the three major factors that affect karst collapse in the study area; (3) by simulating the development of karst caves and the bearing capacity of the karst roof in the goaf structure under different conditions, it is recommended that only civil buildings with not more than three floors can be built in the village. Overburdened soil thicknesses between 6 and 10 m and civil buildings with heights less than 6 m are not suitable parameters for construction activities. If there are hidden soil holes under the overburden layer, dynamic consolidation needs to be applied in order to destroy the structure of the soil layer and to ensure the safety of personnel.

1. Introduction

Generally, researchers consider natural resources as the sum of natural environmental factors that exist naturally and have the use value [1–3]. Mineral resources, as a significant natural resource, have a crucial impact on the economic and social development of China [4]. Mineral resources reserves are the basis for the development of the mining sector and industrialization. China is particularly rich in coal deposits and is one of the world's leading countries in the exploitation of coal resources [5]. However, with the remarkable improvement of China's social and economic development indices, the scale and intensity of coal mining activities [6] have gradually increased [7]. The continuous demand for raw materials, as well as the overexploitation and unreasonable utilization of coal mines, have caused serious damage to the ecological condition of coal mines, leading to a series of ecological and environmental concerns. The

Figure 1: Geographical position of the Mudengdong village.

geological and environmental problems caused by underground mining are classified into four major categories: geological disasters, aquifer damage, topographic and geomorphological landscape damage, and land resource damage [8–10]. In addition, the existence of overexploitation behavior aggravates the waste of coal resources, damages the regional hydrogeological conditions, and creates environmental geological problems, such as large karst [11–15] areas caused by underground goaf [16].

With the continuous development of China's social economy, issues related to mining and its effects on the environment have become prominent discussion topics in the social and economic domains [17]. In the last years, geological environment problems caused by underground mining have been gaining more and more attention [18–22], and it is urgent to take appropriate safety protection measures, such as anchor reinforcement in mining areas [23, 24]. Ecological environment protection and management of coal mining areas have become a problem that needs to be solved at present [25–27]. The Mudendong village [28, 29] in the Gejiu city, Honghe Prefecture, Yunnan Province, is located in the center of the Laochang mining area. Since the 1950s, there have been ongoing underground mining activities around the village. During the last years, wall cracks and ground collapse incidents have appeared in the Mudengdong village. Consequently, local villagers are unable to build new houses because of the karst collapse phenomenon. In 2016, a 4.7 earthquake magnitude in Gejiu created three new collapse sites and damaged several houses in the Mudengdong village. The villagers were forced to choose other locations for post-earthquake recovery and the reconstruction of their homes.

Therefore, the study on the corresponding mechanical properties of rock [30–32], the development and evolution of karst, the formation mechanism of karst collapse, the stability of karst sites, and their prevention and control is of great importance to the housing construction sector in the Mudengdong village. This provides a theoretical basis for the selection of the housing site. The study of the karst collapse phenomenon in this area can be used as a guidebook for understanding the process of karst development and the direction of surface evolution in Gejiu.

2. Overview of Regional Projects

2.1. Analysis of Engineering Geological Conditions

2.1.1. Topography and Geomorphic Features. The Mudengdong village is located about 3 km to the west of Laochang city. Residential houses in the Mudengdong village are located in the lower altitude areas of the basin and are surrounded by mountains. The north and east peaks have a higher elevation than the south and west peaks (Figure 1), while the elevation of the basin surrounded by the mountain ranges varies between 2296.0 and 2300.0 m. The basin has predominant south to north orientation, and the original topography in the northern and southern parts of the basin is a relatively closed karst depression.

2.1.2. Geological Structure. The study area is characterized by the presence of several fault structures that are predominantly crustal faults. The known faults can be divided into two types: the first type is a long-term large-scale deep crustal fault, such as the Honghe fault and Beiyinshan fault; the second type is represented by the syndepositional faults that inherit the intermittent activity of the basement, such as the Mile-Shizong, the Kaiyuan-Qiubei, the Wenshan-Malipo, and the Guangnan-Funing fault zones. The major faults can be divided into four groups based on their extension direction: NE, NW, SN, and EW. The most important structures from the study area include the Honghe fault, the Beiyinshan fault, the Xiaojiang fault, the Ailaoshan fault zone, and the Mile-Shizong fault zone, and the karst development in the study area is mainly controlled by the Beiyin mountain fault, as illustrated in Figure 2.

2.1.3. Stratigraphy. The outcrops in the study area are characterized by quaternary residual slope accumulation sediments (Q_4^{el+dl}), artificial accumulation deposits (Q_4^{ml}),

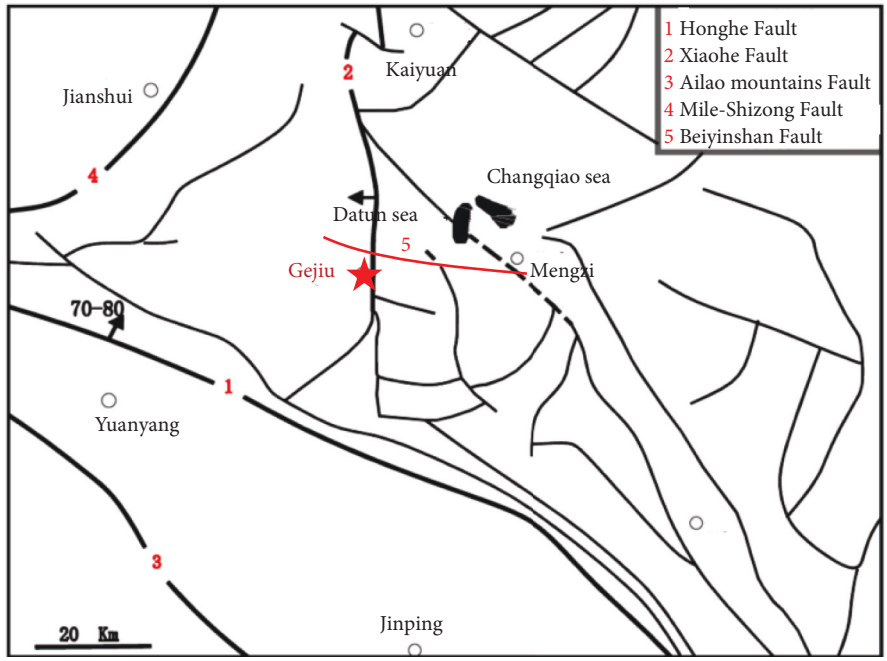

Figure 2: Simplified structural map of the study area.

and the Middle Triassic Gejiu Formation (T_2g_1). Dolomite is the predominant lithotype and the main ore host rock in the Gejiu mining area (Figure 3). Quaternary residual slope deposits are represented by brownish-red and brownish-yellow-red clays. Artificial accumulation sediments are mainly tailing chalk, tailing chalk sand, and tailing chalky clay. The Middle Triassic Gejiu Formation is composed of thick layers of limestone, dolomitic limestone, and dolostone, with a predominant gray color. Karst is strongly developed. The surfaces of the rocks are smooth or parallel and radial "U" grooves are formed by dissolution. The karst types that form on the ground include karst depression, karst ditch, small karst cave, and karst fissure, while the karst types that form in the underground include karst fissure and karst cave.

2.1.4. Major Historical Earthquakes. Based on the statistics of historical seismic data in the Gejiu area, from 1500 to 1980, there were 4 earthquakes with a magnitude of 5~5.5. All epicenters were recorded in the north-south fault zone. According to the "Code for seismic design of buildings" (GB50011-2010) and the "Seismic ground motion parameters zonation map of China" (GB18036-2015), the basic seismic intensity in the study area is level VII, the designed basic seismic acceleration value is 0.15 g, and the characteristic period of the response spectrum is 0.45 s, which indicates that the region is located within a relatively stable region of the crust.

2.2. Characteristics of Karst Development and Its Formation Mechanism

2.2.1. Geological Investigation of Karst. Engineering geological mapping was applied to describe the current karst structure and distribution in the Mudengdong village. A high-density electrical survey was used to identify karst within 50 m below the surface, and an electrical survey was used to detect karst within 180 m below the surface. These methods provided data to support the analysis of underground karst development.

According to the statistics of the karst geological survey, there are 16 karst collapse points (or funnels) (Figure 4), 2 water-falling caves, and 2 karst depressions in the study area. The main morphological characteristics of the karst collapse points are indicated in Table 1.

2.2.2. Conditions of Karst Development. The basic conditions for karst development are as follows: (1) soluble rocks; (2) permeable rocks; (3) erosive water; (4) constant motion of water in the rocks.

Carbonate rocks are widely distributed in the study area, which represents the fundamental requirement for karst development. The regional tectonic conditions are complex, and the unusually complicated tectonic activity causes the rock body to become more fractured, with numerous fissures and strong permeability. The study area has a subtropical plateau monsoon climate with high levels of rainfall. The atmospheric precipitation is unsaturated water, and the groundwater formed by the infiltration of this water becomes erosive. Additionally, the groundwater cycle in the study area is stronger.

Regarding the four basic conditions for karst development, conditions (1) and (2) have a relation to the lithological characteristics and the geological setting, while conditions (3) and (4) mainly depend on the hydrogeological and geomorphic conditions. The lithological characteristics are straightforward. The karst development mechanism in the study area is discussed in the following sections from the aspects of geomorphology, hydrogeology, and geological structure.

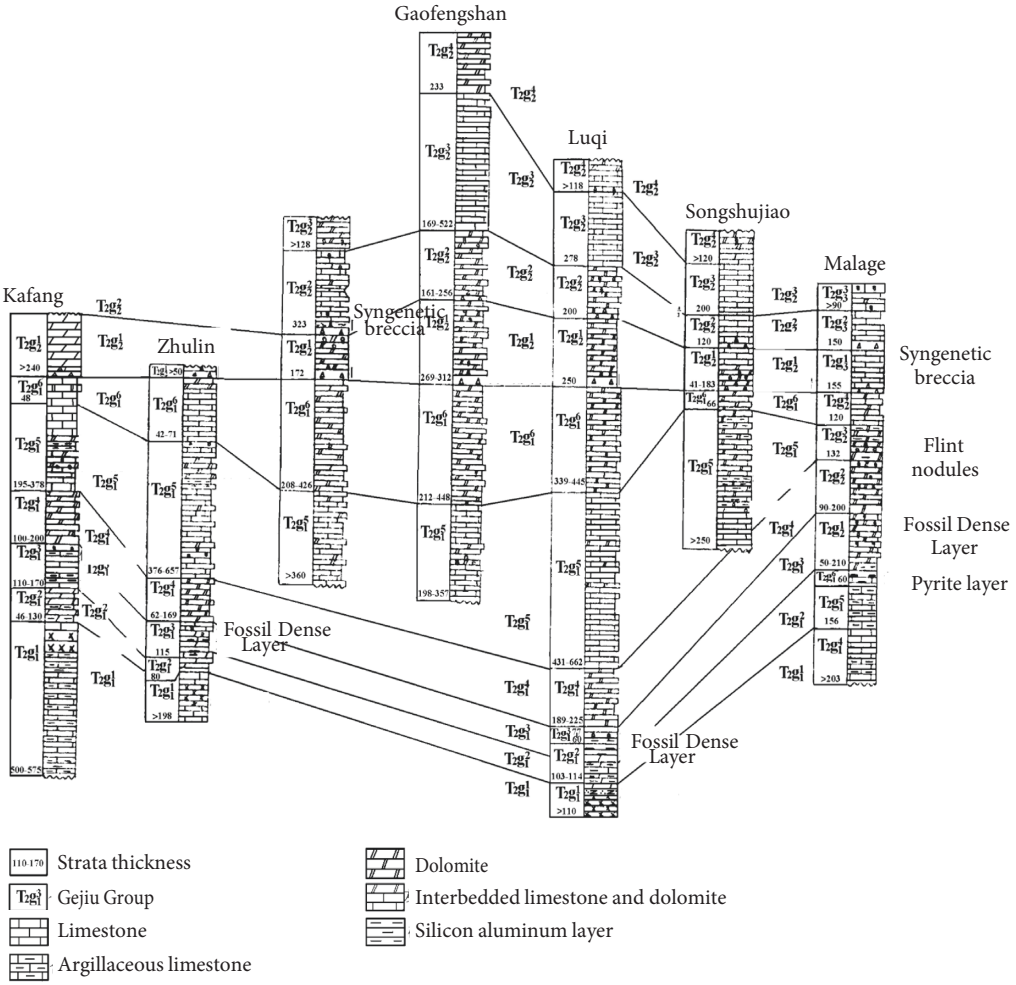

Figure 3: Correlation scheme for the geological sections of the Gejiu group.

Figure 4: Morphological characteristics of karst collapse points and water-falling caves.

Table 1: Features of the karst collapse points (or funnels) in the study area.

Observation point	Location	Morphology and characteristics	Causes
LT1	Gentle slope platform	An ellipse with a length of 2 m and a width of 3 m, and a vertical settlement of 1.5 m	Dissolution, mainly by surface rainwater infiltration
LT9	Foot of slope	An ellipse with a length of 0.5 m and a width of 0.4 m, and a vertical settlement of 0.9 m	Dissolution, but predominantly induced by earthquakes
LT5	Gentle slope platform	An ellipse with a length of 4 m in length and a width of 3 m, and a vertical settlement of 2-3 m	Dissolution, but predominantly induced by earthquakes
LT8	A basin surrounded by mountains on all sides	An ellipse with a length of 0.5 m and a width of 0.4 m, and a vertical settlement of 0.5 m	Dissolution, mainly by surface rainwater infiltration
LT15	Foot of the halfway hill slope	An oval shape with a length of 1.5 m and a width of 0.8 m, and a depth of about 8m	Dissolution, mainly by surface rainwater infiltration

Table 2: Karst development degree characteristics and indicators.

Karst development degree	Karst phenomenon	Karst density (number/km^2)	Maximum spring flow (l/s)	Karst rate of boreholes (%)
Extremely intense	Surface: a large cave Underground: a large-scale underground river system dominated by piped water	>15	>50	>10
Intense	Surface: karst caves, sinkholes, funnels, and depressions Underground: smaller-scale underground river, mainly containing pipe water and some fissure water	5~15	10~50	5~10
Moderately intense	Surface: small scale caves, additional sinkholes, and funnels Underground: fissure-shaped underground river, dominated by fissure water	1~5	5~10	2~5
Faint	Numerous dissolved fissures, a small number of sinkholes, funnels and karst springs, and multilayered aquifers dominated by fissure water	0~1	<5	<2

2.2.3. Strength of Karst Development. The most common indicators used to determine the degree of karst development are as follows: (1) karst phenomenon; (2) karst density (number of karst points per square kilometer); (3) the karst rate of drilled holes; and (4) the flow rate of dark rivers or springs. The classification has four levels: extremely intense, intense, moderately intense, and faint (Table 2).

2.3. Mechanism of Karst Collapse Genesis

2.3.1. Analysis of Karst Collapse Factors. The formation of karst collapse is generally influenced by several factors. In different areas, the same factors may lead to distinct karst collapse results, while human activities and natural factors are also important elements that induce collapse. Based on the previously mentioned development mechanism and conditions in the Mudengdong village, the main factors that may lead to karst collapse are discussed below.

(1) Collapse caused by surface rainwater infiltration: in the study area groundwater is encountered at great depths. The minimum depth is equal to 188m, which indicates that the possibility of karst collapse caused by the fluctuation of the groundwater level is not substantial. Therefore, the infiltration of surface rainwater is one of the main factors of karst collapse [33].

(2) Collapse caused by vibrations or earthquakes: an earthquake produces seismic waves that induce the shaking of rocks and soils, thus causing the rock to fracture. Karst development is strong in the study area, and formed soil caves can easily collapse under the action of vibrations or earthquakes.

(3) Collapse caused by loading: the influence of human activities is much smaller compared to the damage done by earthquakes, but karst collapse can still be induced without difficulty under certain conditions and circumstances. The construction of buildings adds additional load to the top plate of the karst or the earth's cave, which will cause the karst to collapse if it exceeds the bearing capacity of the earth's cave vault. Therefore, the damage to the roof plate caused by the generated external load leads to the collapse of the karst.

(4) Rainfall, snowfall, and other triggering factors: snowfall is an important factor that increases groundwater activity through surface descent and recharge of the groundwater surface. The specific mechanisms that promote karst collapse are as follows:

(a) Rainfall saturates the geotechnical body, increases its capacity, modifies the hard plastic state of the soil, reduces the angle of internal

friction and cohesion, and thus decreases its strength

(b) Heavy snowfall or rainfall increases the thickness of the roof of the soil cover, resulting in collapse

(c) The infiltration of surface water increases the content of electrolytes, which eventually leads to changes in the physical and mechanical properties of the soil layer

(d) Rainfall or snowfall steadily leads to the rise of groundwater levels, resulting in positive pressure in the karst space and negative pressure caused by the rapid flow of the groundwater in the runoff zone

(e) Karst collapse induced by underground drainage is not considered because the groundwater level is encountered at great depths

2.3.2. Analysis of Karst Collapse Mechanism. The karst collapse mechanism is more complex and includes the latent erosion effect, the vacuum erosion effect, the pressure difference effect, the vertical seepage effect, the self-gravity effect, the buoyancy effect, the soil strength effect, the earthquake or vibration effect, and the load effect. The subduction effect, the vacuum erosion effect, the pressure difference effect, and the buoyancy effect are associated with the collapse mechanism caused by the fluctuation of groundwater levels. However, the minimum depth at which groundwater is encountered in the study area is approximately 188 m, indicating that collapse caused by these four mechanisms is not applicable. Therefore, the study area is mainly related to the vertical seepage effect, the self-gravity effect, the soil strength effect, the earthquake or vibration effect, the load effect, and other collapse mechanisms.

(1) Self-gravity effect: the self-gravity effect results in soil cave collapse due to gravity. The gravity effect caused by the self-weight of the rock mass or the external load destroys the karst roof, peeling off layer by layer, resulting in the process and phenomenon of collapse, labeled as gravity-induced collapse.

(2) Vertical seepage effect: the vertical seepage pressure effect is caused by the infiltration of surface waters derived from rainfall and snowfall. The seepage pressure effect refers to the various combined effects on the cover soil produced by the upper action of infiltration recharge of karst groundwater, such as rainfall or surface water. The collapse points LT3, LT10, LT12, and LT15 in the study area are created by surface water runoff. Their formation mechanism is that after being subjected to infiltration, water moves in the pore space and exerts vertical infiltration pressure on the particles, thus changing the mechanical properties of the soil. When the infiltration pressure reaches a certain value, the structure of the soil is rapidly destroyed and the soil particles follow the water flow to move, resulting in the flow soil phenomenon and, consequently, the collapse of the ground.

(3) Earthquake or the vibration effect: the collapse of the LT5 and LT8 points in the study area was induced by several earthquakes that happened in May 2016 with a maximum magnitude of 4.7. Vibrations can also produce fluctuations and damage the soil cavity by direct impact. Therefore, under the action of earthquakes or vibrations, the strength of the overlying soil layer is reduced and exposed to the destructive effects of the shock waves, which diminishes the collapse resistance of the soil arch and leads to collapse.

(4) Load effect: in the karst collapse area, building loads, vehicle loads, pedestrian loads, and impact loads may cause the karst ground to collapse, since such loads exert pressure in the vertical direction. The top arch of the karst soil caves collapses because it cannot withstand its gravity and the vertical pressure exerted by the external loads.

3. Numerical Simulation of Cave Stability

3.1. Generalization and Establishment of the Geological Model. The study of geological data from the Mudengdong village indicates that quaternary red clay is widely distributed in the area, and the soil cave collapse in the red clay layer accounts for more than 30%. Therefore, the soil hole development was considered to be located near the contact surface between the red clay layer and the tuff layer.

The present numerical simulation [34, 35] model generalizes the caves into circular soil caverns and funnel-shaped soil caverns, without considering the effects of accumulation and filling during the simulation process. By analyzing the statistical analysis data of 16 karst collapse points (or funnels) developed in the study area, the size of the calculation model was defined as a 50 m × 20 m rectangle. The diameter of the circular soil holes is 3 m, the width of the upper part of the funnel-shaped soil holes is 4 m, the width of the lower part is 3 m, and the depth is 2 m. According to the geophysical data, it can be concluded that the quaternary overburden layer is relatively thin in the other parts of the cavern. However, there are some areas where the overburden layer is thick, which cannot form a stable roof support arch. Combined with the actual geological field mapping data, the thickness of the overlying soil layer in the area where soil holes occur usually ranges between 0.5 and 6 meters. Most of the overlying soil layer thickness is less than 10 meters, and only in some rare cases detected by geophysical exploration techniques, the overlying soil layer thickness is over 20 meters. The thickness H of the overburden soil layer was set to $H = 3$ m, $H = 4$ m, $H = 6$ m, $H = 8$ m, and $H = 10$ m, respectively, for the corresponding numerical simulations. The plane42 2-D solid structural element model was used for the rock and soil mass simulation. Additionally, Drucker–Prager's elastoplastic model, which is commonly used in geotechnical engineering, was also used as shown in Figure 5.

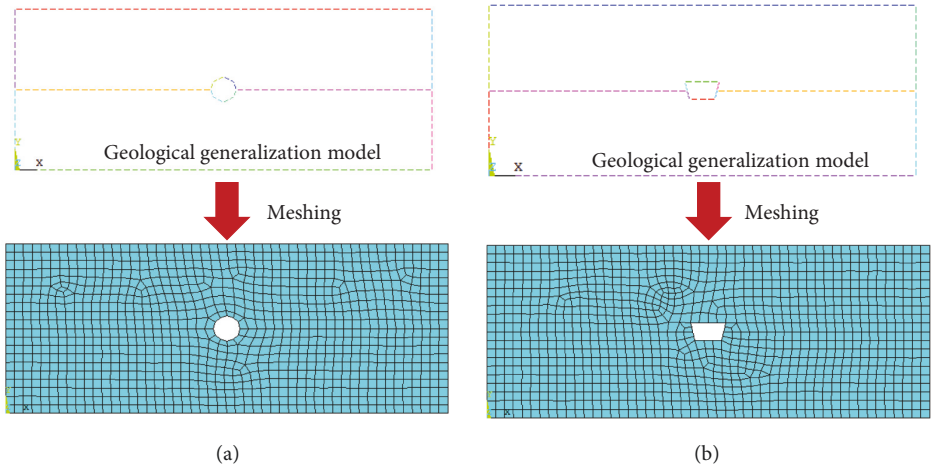

Figure 5: Geological generalization model and grid. (a) Circular soil holes. (b) Funnel-shaped soil holes.

Table 3: Values of the simulation parameters.

Lithology	Cohesion (kPa)	Angle of internal friction (°)	Angle of dilation (°)	Elastic modulus (MPa)	Volumetric Weight (N/cm^2)	Poisson's ratio (υ)
Red clay	30	12	0	30	1900	0.39
Limestone	250	40	10	4000	2400	0.3

3.2. Selection of Model Calculation Parameters and Boundary Conditions. For the Drucker–Prager model, the required data parameters include density, elastic modulus, Poisson's ratio, internal friction angle, cohesion, and angle of dilation. The parameter values for this study are shown in Table 3.

In order to make the model closer to the actual situation, certain restrictions must be set in the model truncation surface, that is, the corresponding boundary conditions must be set so that the equilibrium equations can be solved accordingly. This paper is focused on stability under static conditions. When setting boundary conditions, the y-axis constraint is set at the bottom of the model and the x-axis constraint is set to the left and right directions of the model.

3.3. Selection of the Load. The soil in the upper part of karst is subjected to gravity or external load, which increases its self-weight effect. The upper support arch of the soil cannot handle its balance requirements, which leads to the collapse of the overlying soil layer of red clay into the cavern and forms a funnel running up and down.

It is mentioned in the research report that the main causes of karst collapse in the Mudengdong village are vibrations induced by blasting during mining operations, earthquakes, and the direct compression failure of the soil cave caused by the load of buildings exceeding the roof arch. During the past years, mining operations have been regulated by the government, while the action of earthquakes is accidental. Therefore, these causes are not included in the numerical simulation calculations. In this study, it is considered that the soil cave is directly destroyed when the building load exceeds the bearing capacity of the soil cave vault, which leads to the collapse of the soil cave. The building load is simplified as a uniformly distributed load, and the numerical calculation of the uniformly distributed load is described below.

Since most of the houses built in the Mudengdong village are civilian buildings, the proposed house size is 10 m × 10 m, the floor height is 3 m, the wall thickness is 0.3 m, the floor thickness is 0.1 m, and the ceiling thickness is 0.3 m.

The uniform load value of a one-storey building is expressed as

$$G_1 = \gamma V_1 = \frac{25\,\text{kN}}{\text{m}^3} \times 73.72\text{m}^3 = 1843\,\text{kN},$$
$$q_1 = \frac{G_1}{S} = \frac{1843\,\text{kN}}{100\,\text{m}^2} = 18.43\,\text{kPa}. \quad (1)$$

The uniform load value of a two-storey building is expressed as

$$G_2 = \gamma V_2 = \frac{25\,\text{kN}}{\text{m}^3} \times 64.92\,\text{m}^3 = 1623\,\text{kN},$$
$$q_2 = \frac{G_2}{S} = \frac{1623\,\text{kN}}{100\,\text{m}^2} = 16.23\,\text{kPa}, \quad (2)$$
$$q = q_1 + q_2 = 34.66\,\text{kPa}.$$

The uniform load value of a three-storey building is expressed as

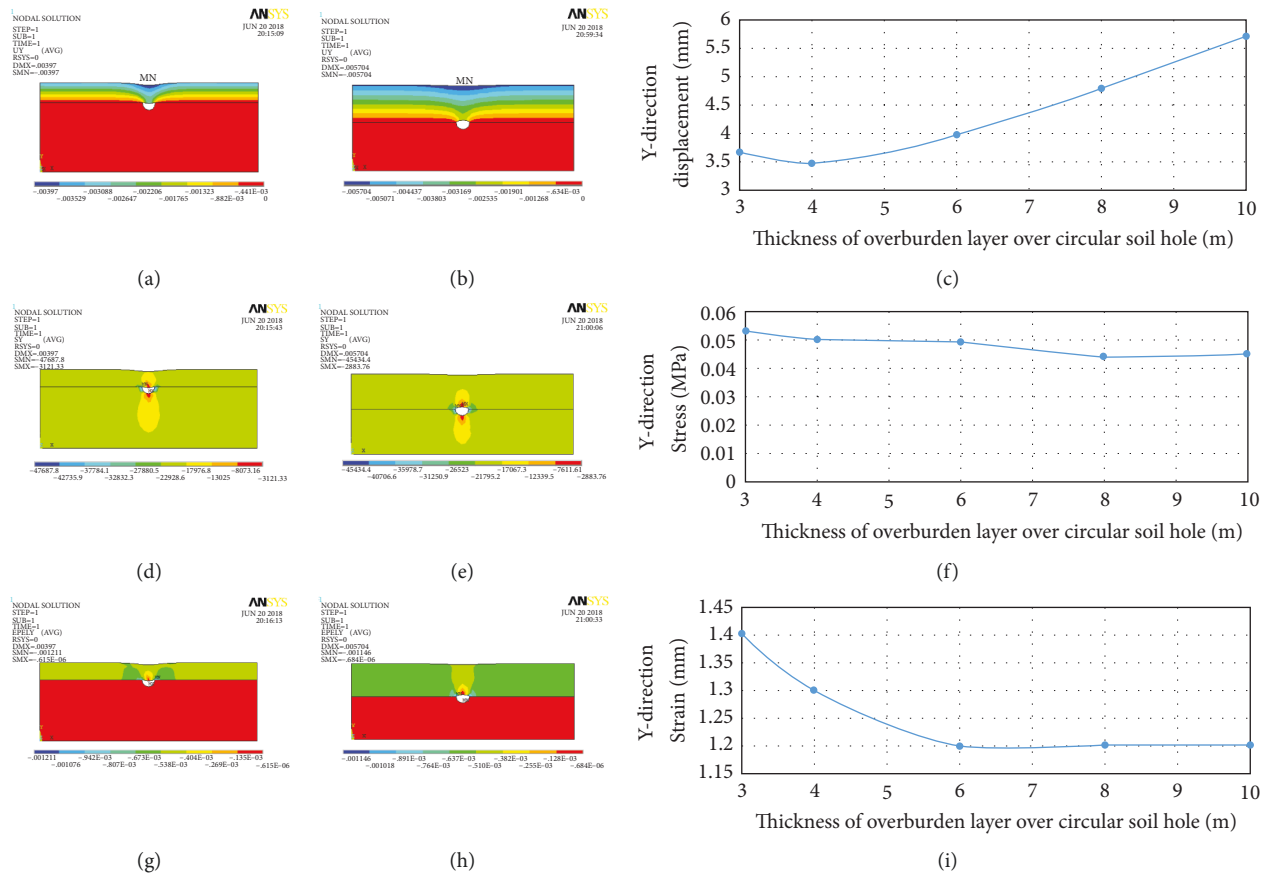

Figure 6: $q = 18.43$ kPa scenario. Results of displacement cloud map: (a) $H = 6$ m and (b) $H = 10$ m; (c) displacement curve; stress cloud map: (d) $H = 6$ m and (e) $H = 10$ m; (f) stress curve; strain cloud map: (g) $H = 6$ m and (h) $H = 10$ m; (i) strain curve.

$$G_3 = \gamma V_3 = \frac{25\,kN}{m^3} \times 64.92\,m^3 = 1623\,kN,$$
$$q_3 = \frac{G_3}{S} = \frac{1623\,kN}{100\,m^2} = 16.23\,kPa, \quad (3)$$
$$q = q_1 + q_2 + q_3 = 50.89\,kPa.$$

3.4. Numerical Simulation Results and Analysis

3.4.1. Numerical Simulation of Circular Soil Holes under Different Loads. According to the research report, the thickness of the overlying soil layer in the area where the soil holes occur usually ranges between 0.5 and 6 meters, while most of the overlying soil layer thickness is less than 10 meters. Only a few parts of the soil layer with thicknesses greater than 20 meters have been detected by geophysical prospecting. The thickness of the overlying soil layer H is set to $H = 3$ m, $H = 4$ m, $H = 6$ m, $H = 8$ m, and $H = 10$ m, respectively. Three different scenarios where the uniform load value q is set to $q = 18.43$ kPa, $q = 34.66$ kPa, and $q = 50.89$ kPa, respectively, were used for numerical simulation models to obtain the corresponding displacement, stress, and strain values. The simulation results are discussed below.

(1) $q = 18.43$ kPa: according to Figures 6(a) and 6(b), when the thicknesses of the overlying soil layer H are 6 m and 10 m, then the obtained displacement values are 3.97 mm and 5.7 mm, respectively. There is an obvious displacement at the roof of the soil cavern, and it increases with the upward trend. The large displacement of the soil cave concentrates in the vertical direction of the roof and presents a symmetrical distribution. Under the same load, it can be observed from Figure 6(c) that a thicker overburden layer causes greater surface displacement values. However, the increase in the soil layer thickness makes the soil tunnel to be more stable. If the soil is thinner, then the probability of collapse increases. Figures 6(f) and 6(i) indicate that stress and strain tend to significantly decrease with the increase of the soil thickness. The area with large stress values is primarily concentrated around the soil cave body, which is compressive stress, with values equal to 0.049 MPa and 0.045 MPa. The strain occurs predominantly in the upper part of the soil layer. The strain concentrated in the soil tunnel roof arch part has a value of 1.2 mm.

(2) $q = 34.66$ kPa: according to Figures 7(a) and 7(b), when the thicknesses of the overlying soil layer H are 6 m and 10 m, then the obtained displacement values

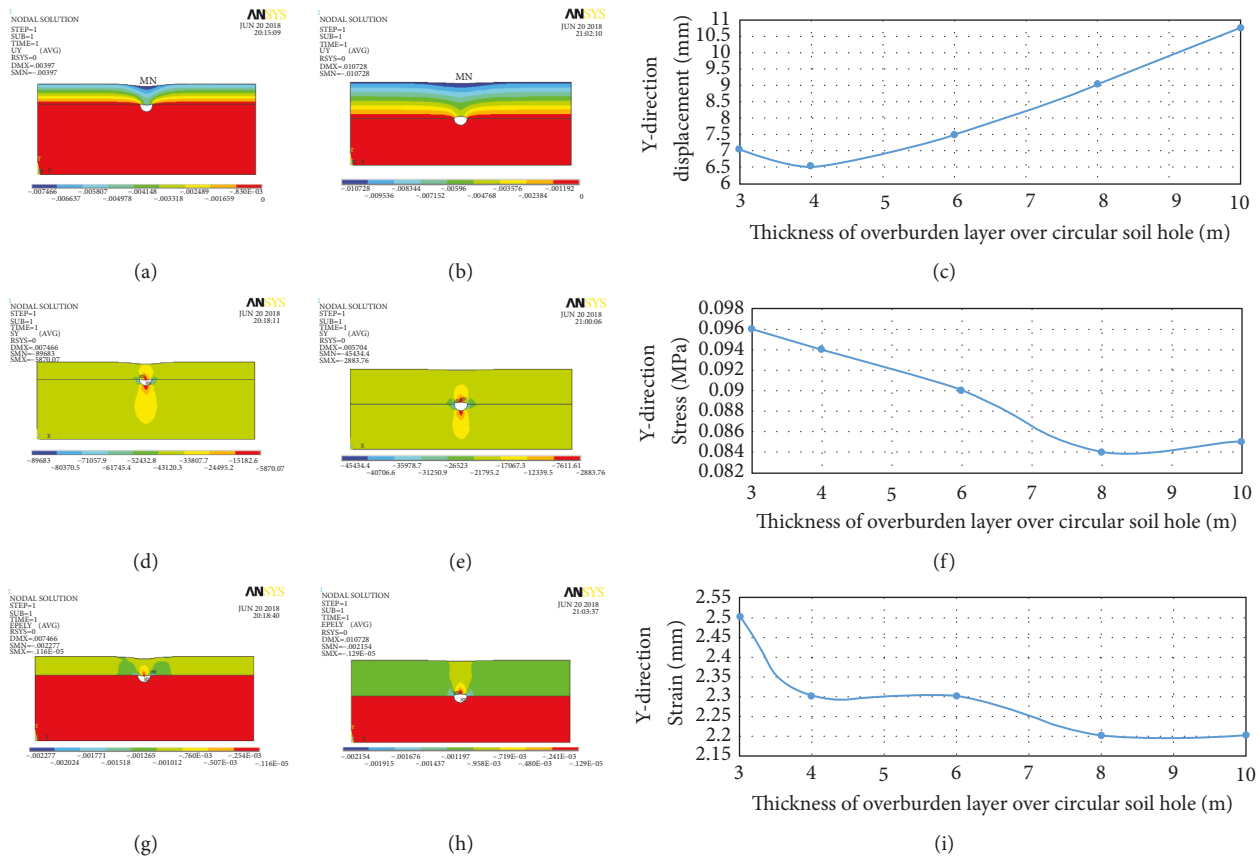

FIGURE 7: $q = 34.66$ kPa scenario. Results of displacement cloud map: (a) $H = 6$ m and (b) $H = 10$ m; (c) displacement curve; stress cloud map: (d) $H = 6$ m and (e) $H = 10$ m; (f) stress curve; strain cloud map: (g) $H = 6$ m and (h) $H = 10$ m; (i) strain curve.

are 7.47 mm and 10.73 mm, respectively. There is an obvious displacement at the roof of the soil cavern, and it increases with the upward trend. The large displacement of the soil cave concentrates in the vertical direction of the roof and presents a symmetrical distribution. Under the same load, it can be observed from Figure 7(c) that a thicker overburden soil layer generates greater surface displacement values. However, the increase in the soil layer thickness causes the soil tunnel to be more stable. If the soil is thinner, then the likelihood of collapse increases. Figures 7(f) and 7(i) indicate that stress and strain tend to decrease with the increase of the soil thickness. The area with larger stress values is primarily concentrated around the cavity of the soil, which is compressive stress, with values of 0.09 MPa and 0.085 MPa. The strain occurs predominantly in the upper part of the soil layer. The strain concentrated in the top arch part of the soil cavern has strain sizes of 2.3 mm and 2.2 mm. Based on the comparisons from Figure 7, it can be inferred that the displacement, the stress, and the strain of the same overlying soil layer are directly correlated with the load increase.

(3) $q = 50.89$ kPa: according to Figures 8(a) and 8(b), when the thicknesses of the overlying soil layer H are 6 m and 10 m, then the obtained displacement values are 11.29 mm and 15.89 mm, respectively. There is an obvious displacement at the roof of the soil cavern, and it increases with the upward trend. The large displacement of the soil cave concentrates in the vertical direction of the roof and presents a symmetrical distribution. Under the same load, it can be observed from Figure 8(c) that a thicker overburden soil layer creates greater surface displacement values. However, the increase in the soil layer thickness causes the soil tunnel to be stable. If the soil is thinner, then the probability of collapse increases. Figures 8(f) and 8(i) suggest that stress and strain tend to significantly decrease with the increase of the soil thickness. The area with large stress values is primarily concentrated around the soil cave body, which is compressive stress, with values of 0.094 MPa and 0.087 MPa. The strain predominantly occurs in the upper part of the soil layer, and the large strain concentrated in the soil tunnel roof arch part has a value of 2.6 mm. Based on the comparisons from Figure 8 it is clear that the displacement, the stress, and the strain of the same overburden tend to increase with the load increase.

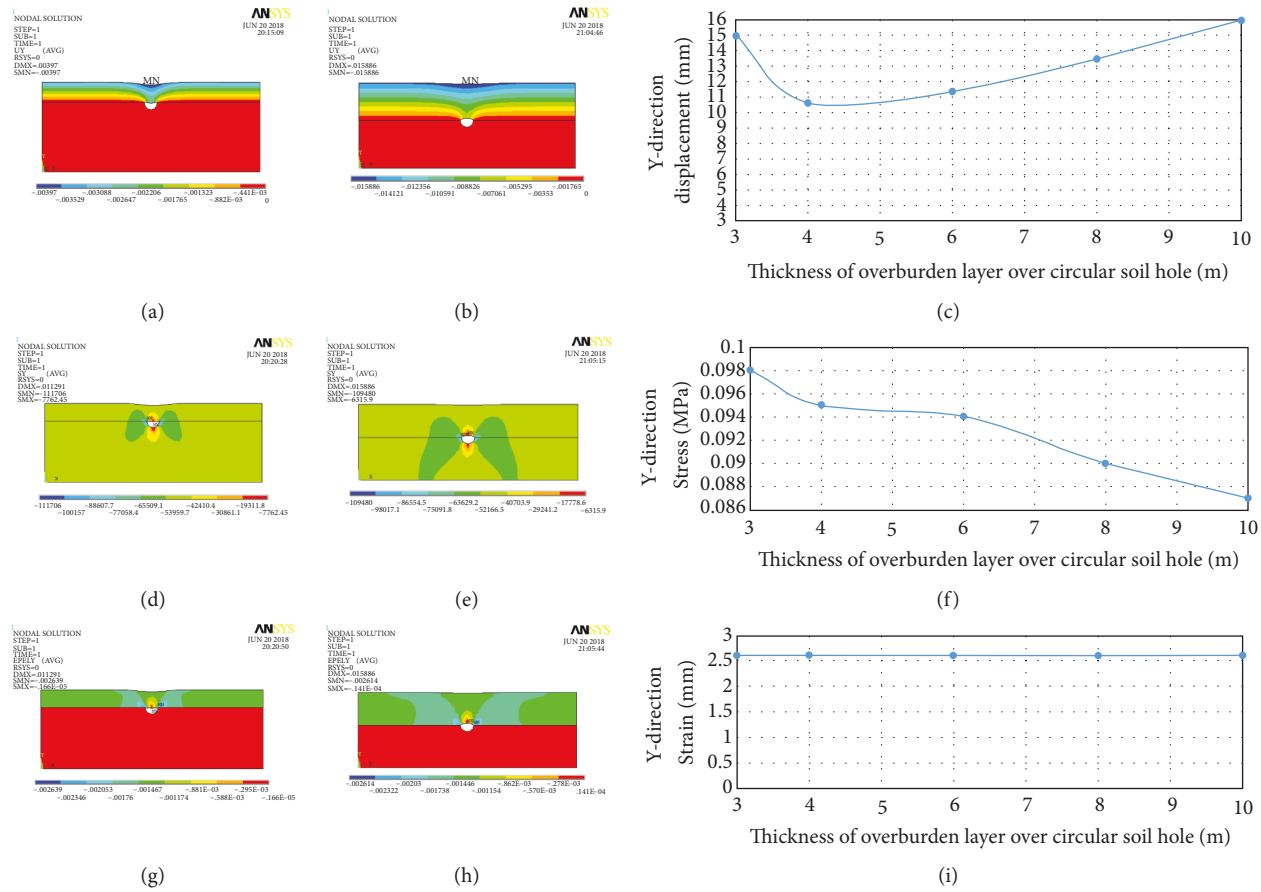

FIGURE 8: $q = 50.89$ kPa scenario. Results of displacement cloud map: (a) $H = 6$ m and (b) $H = 10$ m; (c) displacement curve; stress cloud map: (d) $H = 6$ m and (e) $H = 10$ m; (f) stress curve; strain cloud map: (g) $H = 6$ m and (h) $H = 10$ m; (i) strain curve.

3.4.2. Numerical Simulation of Funnel-Shaped Soil Holes under Different Loads. Based on the study report results, the thickness of the overlying soil layer in the area where the funnel-shaped soil hole occurs ranges between 0.5 m and 6 m, while in most of the other parts the thickness of the overlying soil layer is less than 10 m. The rare spots where the soil layer is exceeding 20 meters were identified by geophysical exploration methods. The thickness H of the overlying soil layer is considered as $H = 3$ m, $H = 4$ m, $H = 6$ m, $H = 8$ m, and $H = 10$ m, respectively. Three different scenarios where the uniform load value q is set to $q = 18.43$ kPa, $q = 34.66$ kPa, and $q = 50.89$ kPa, respectively, were selected as the house building load for the corresponding numerical simulation model to obtain the corresponding displacement, stress, and strain values.

(1) $q = 18.43$ kPa: according to Figures 9(a) and 9(b), when the thicknesses of the overlying soil layer H are 6 m and 8 m, then the obtained displacement values are 4.76 mm and 5.33 mm, respectively. There is an obvious displacement at the roof of the soil cavern, and it increases with the upward trend. The large displacement of the soil cave concentrates in the vertical direction of the roof and presents a symmetrical distribution. Under the same load, it can be observed from Figure 9(c) that a thicker overburden soil layer causes greater surface displacement values. However, the increase in the soil layer thickness makes the soil tunnel to be more stable. If the soil is thinner, then the probability of collapse increases. Figures 9(f) and 9(i) indicate that stress and strain tend to decrease significantly with the increase of the soil thickness. The area with the largest stress values is primarily concentrated around the soil cave body, which is the compressive stress, with values of 0.039 MPa and 0.037 MPa. The strain occurs predominantly in the upper part of the soil layer, and the larger strain concentrated in the top arch of the soil tunnel has strain sizes of 1.3 mm and 1.2 mm.

(2) $q = 34.66$ kPa: according to Figures 10(a) and 10(b), when the thicknesses of the overlying soil layer H are 6 m and 8 m are 8.98 mm and 10.02 mm, respectively. There is a more obvious displacement at the top of the soil cavern, and it increases as it goes up. The larger displacement of the soil hole is concentrated in the vertical direction of the top of the hole and has a symmetrical distribution. Under the same load, it can be observed from Figure 10(c) that a thicker upper cover soil layer generates greater displacement values. However, the increase in the soil layer thickness causes the soil hole to be more stable. If the

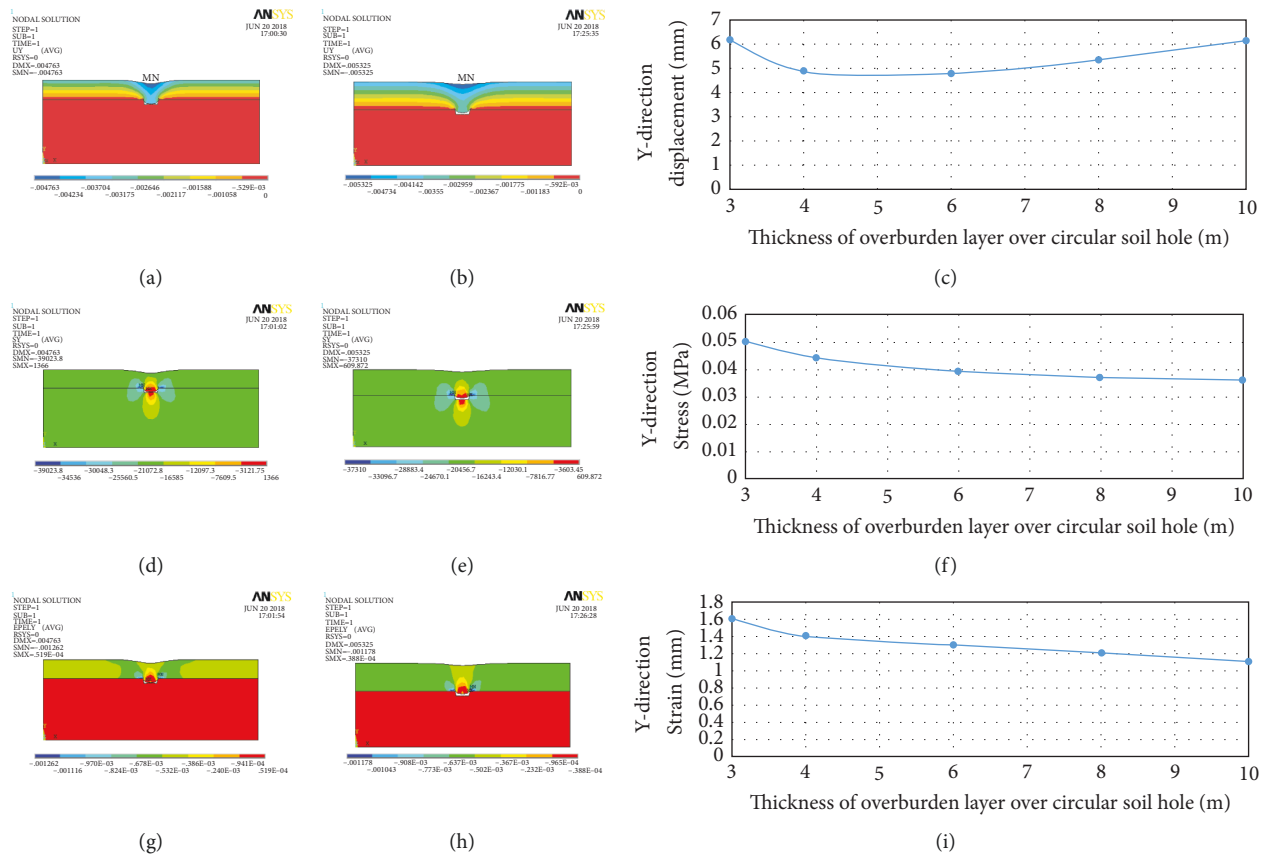

FIGURE 9: $q = 18.43$ kPa scenario. Results of displacement cloud map: (a) $H = 6$ m and (b) $H = 10$ m; (c) displacement curve; stress cloud map: (d) $H = 6$ m and (e) $H = 10$ m; (f) stress curve; strain cloud map: (g) $H = 6$ m and (h) $H = 10$ m; (i) strain curve.

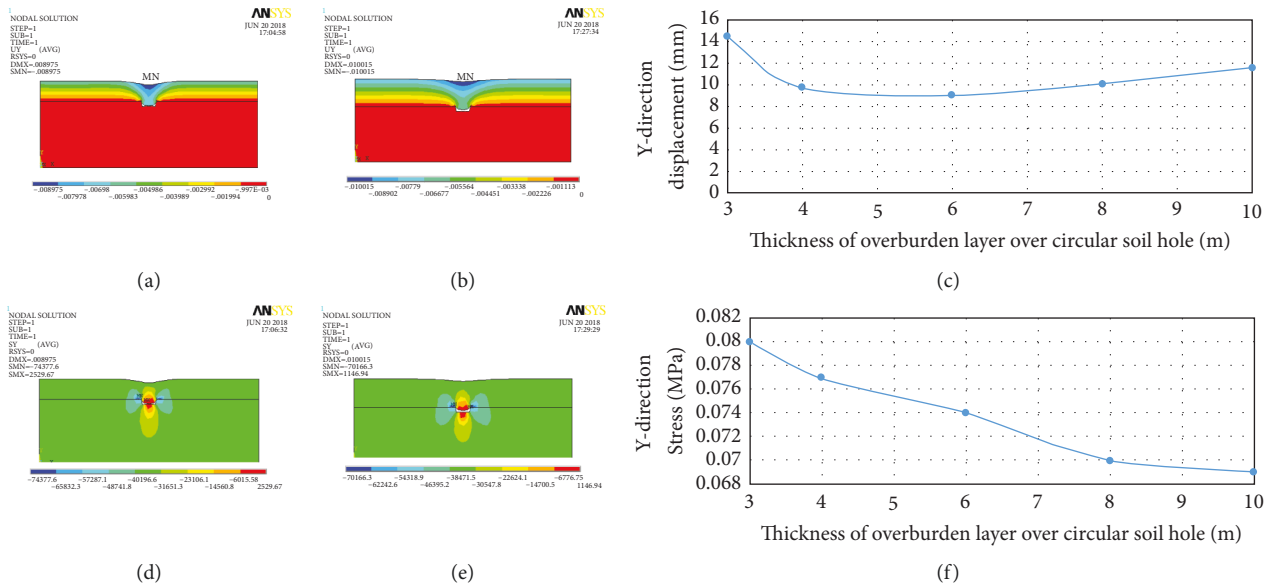

FIGURE 10: Continued.

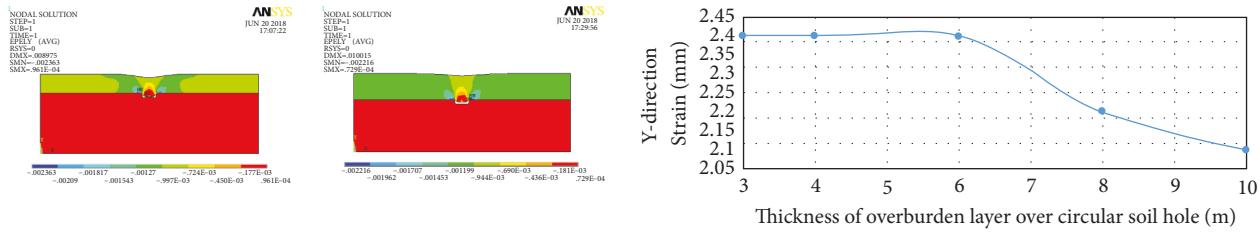

FIGURE 10: $q = 34.66$ kPa scenario. Results of displacement cloud map: (a) $H = 6$ m and (b) $H = 10$ m; (c) displacement curve; stress cloud map: (d) $H = 6$ m and (e) $H = 10$ m; (f) stress curve; strain cloud map: (g) $H = 6$ m and (h) $H = 10$ m; (i) strain curve.

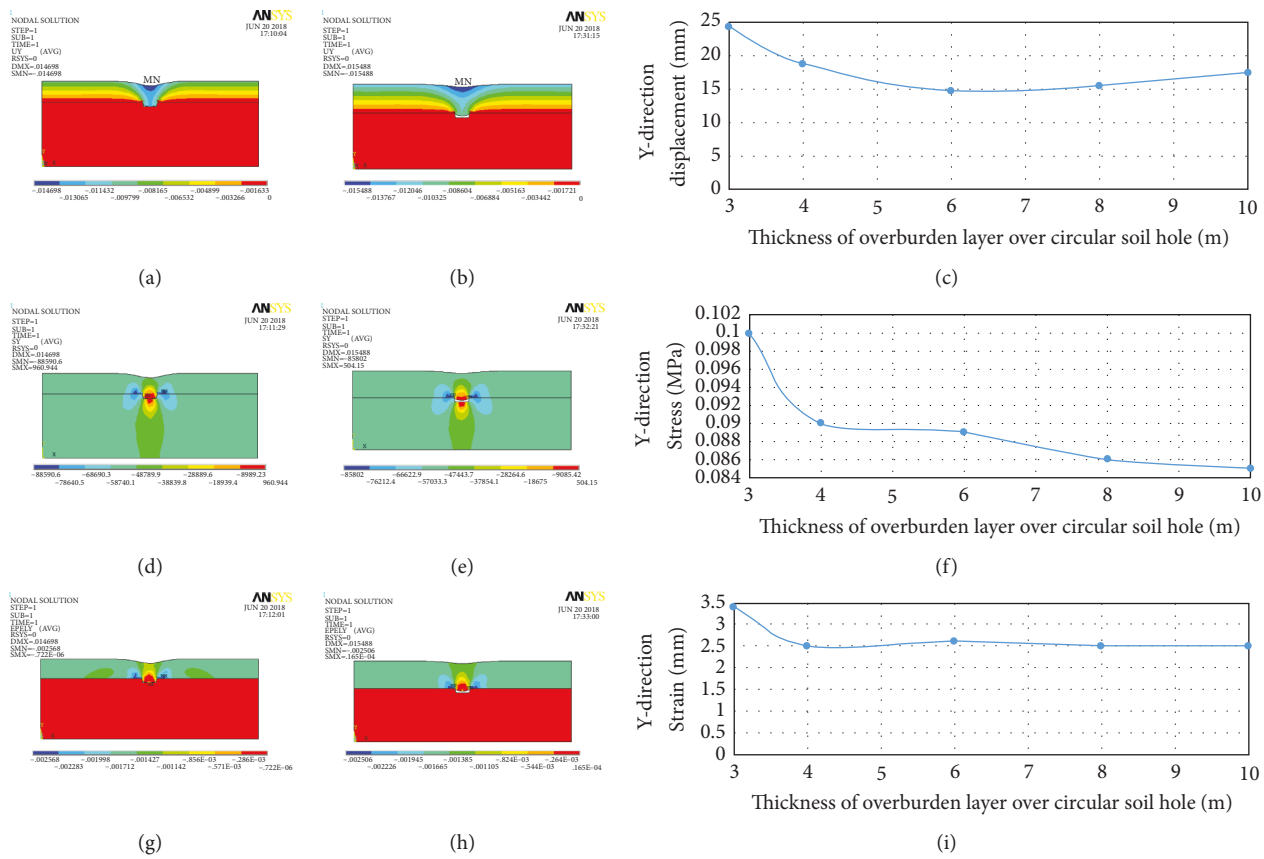

FIGURE 11: $q = 50.89$ kPa scenario. Results of displacement cloud map: (a) $H = 6$ m and (b) $H = 10$ m; (c) displacement curve; stress cloud map: (d) $H = 6$ m and (e) $H = 10$ m; (f) stress curve; strain cloud map: (g) $H = 6$ m and (h) $H = 10$ m; (i) strain curve.

soil layer is thinner, then the likelihood of collapse increases. Figures 10(f) and 10(i) suggest that stress and strain tend to significantly decrease with the increase of the soil thickness. The area with larger stress values is primarily concentrated around the soil cave body, which is compressive stress, with values of 0.074 MPa and 0.070 MPa. The strain occurs predominantly in the upper part of the soil layer. The larger strain concentrated in the roof arch part of the soil tunnel has strain sizes of 2.4 mm and 2.2 mm. Based on the comparisons from Figure 10, it can be concluded that the displacement, the stress, and the strain of the same overburden are directly correlated with the load increase.

(3) $q = 50.89$ kPa: according to Figures 11(a) and 11(b), when the thicknesses of the overlying soil layer H are 6 m and 8 m, then the obtained displacement values are 14.70 mm and 15.49 mm, respectively. There is an obvious displacement at the roof of the soil cavern, and it increases with the upward trend. The large displacement of the soil cave concentrates in the vertical direction of the roof and presents a symmetrical distribution. Under the same load, it can be observed from Figure 11(c) that a thicker overburden

soil layer induces greater surface displacement values. However, the increase in the soil layer thickness causes the soil tunnel to be more stable. If the soil is thinner, then the probability of collapse increases. Figures 11(f) and 11(i) indicate that stress and strain tend to significantly decrease with the increase of the soil thickness. The area with the largest stress values is primarily concentrated around the soil cave body, which is the compressive stress, with values of 0.089 MPa and 0.086 MPa. The strain occurs predominantly in the upper part of the soil layer. The larger strain concentrated in the roof of the soil cavern has strain sizes of 2.6 mm and 2.5 mm. Based on the comparisons from Figure 11, it can be inferred that the displacement, the stress, and the strain of the same overburden tend to increase with the load increase.

4. Conclusion

(1) The karst development in the study area is mainly controlled by the Beiyinshan fault, which is consistent with the strike of the fault. Karst is more developed in the basin, in the foot slope, or in the pass area. The carbonate distribution area within 290 meters below the surface level is a vertical seepage zone, and the karst has a predominantly vertical form in its initial stage of formation. The main factors contributing to karst collapse in the study area are surface rainwater infiltration, vibrations or earthquakes, and load pressure.

(2) The predominant lithologies in the study are represented by two distinct layers: red clay layer and tuff layer. When the thickness of the upper overburden layer is between 6 and 10 m, then one-storey, two-storey, or three-storey civil housing buildings can be built. However, it is not recommended to construct civil buildings when the thickness of the upper overburden layer is less than 6m. The bearing capacity of the foundation in this area is limited; therefore, it is not advisable to build high and large civil constructions.

(3) In some cases, when the thickness of the overburden soil layer is less than 6 m and the soil holes are hidden, the dynamic consolidation method should be applied to destroy the structure of the soil layer, induce the soil holes to collapse artificially, and subsequently take the corresponding safety measures. Civil buildings can be built on the bedrock if the bearing capacity requirements are met. It should be emphasized that the above proposed housing construction scheme can only be adopted on the premise of taking preventive measures for karst collapse.

Data Availability

The data used to support the findings of this study are available from the corresponding author upon request.

Conflicts of Interest

The authors declare that there are no conflicts of interest regarding the publication of this paper.

Acknowledgments

This study was supported by the Science and Technology Program of China Nonferrous Metals Industry Kunming Survey and Design Research Institute Co. (201703) and the Research Projects of China Aluminum International Engineering Corporation Limited (CJ2020JS-12).

References

[1] O. N. Nikolaeva, "On developing of thematic content for the system of natural resources' digital cartographic models of region," *Geodesy and Cartography*, vol. 913, no. 7, 2016.

[2] J. Burger, M. Gochfeld, and M. Greenberg, "Natural resource protection on buffer lands: integrating resource evaluation and economics," *Environmental Monitoring and Assessment*, vol. 142, no. 1-3, pp. 1–9, 2008.

[3] S. Wu, L. Li, and S. Li, "Natural resource abundance, natural resource-oriented industry dependence, and economic growth: evidence from the provincial level in China," *Resources, Conservation and Recycling*, vol. 139, pp. 163–171, 2018.

[4] T. Zhang, "Analysis on the problems and solutions of open pit mining," *World Nonferrous Metals*, vol. 08, pp. 45-46, 2020.

[5] Y. Qin, J. Shen, and R. Shi, "Strategic value and choice on construction of large CMG industry in China," *Journal of China Coal Society*, vol. 47, no. 01, pp. 371–387, 2022.

[6] Q. Wang, M. He, S. Li et al., "Comparative study of model tests on automatically formed roadway and gob-side entry driving in deep coal mines," *International Journal of Mining Science and Technology*, vol. 31, no. 4, pp. 591–601, 2021.

[7] J. W. Teng, J. M. Liu, C. Liu, Y. Jing-jin, H. Li-guo, and Z. Yong-qian, "Prospecting for metal ore deposits in second deep space of crustal interior the building of strategy reserve base of northeast China," *Journal of Jilin University (Earth Science Edition)*, vol. 04, pp. 633–651, 2007.

[8] J. X. Xu, H. Zhao, G. Li, and L. Wu, "Land ecological assessment and its spatial variation in coal mining area," *Journal of China University of Mining & Technology*, vol. 46, no. 01, pp. 192–200, 2017.

[9] N. Liu, X. G. Zhao, S. J. Song, and Z. Wen-Fu, "Effect of Underground Coal Mining on Slope Morphology and Soil Erosion," *Mathematical Problems in Engineering*, vol. 2019, Article ID 5285126, 2019.

[10] C. Cao, W. Zhang, J. Chen, B. Shan, S. Song, and J. Zhan, "Quantitative estimation of debris flow source materials by integrating multi-source data: a case study," *Engineering Geology*, vol. 291, Article ID 106222, 2021.

[11] M. Veress, "Karst types and their karstification," *Journal of Earth Sciences*, vol. 31, no. 3, pp. 621–634, 2020.

[12] C. Jiang, X. Gao, B. Hou et al., "Occurrence and environmental impact of coal mine goaf water in karst areas in China," *Journal of Cleaner Production*, vol. 275, Article ID 123813, 2020.

[13] F. Cui, B. Li, C. Xiong et al., "Dynamic triggering mechanism of the pusa mining-induced landslide in nayong county, guizhou Province, China," *Geomatics, Natural Hazards and Risk*, vol. 13, no. 1, pp. 123–147, 2021.

[14] Y. B. Hu, W. P. Li, X. M. Chen, H. Xu, and S. Liu, "Temporal and Spatial Evolution Characteristics of Fracture Distribution of Floor Strata in Deep Coal Seam Mining," *Engineering Failure Analysis*, vol. 132, 2022.

[15] A. Li, Q. Ma, Y. Lian, L. Ma, Q. Mu, and J. Chen, "Numerical simulation and experimental study on floor failure mechanism of typical working face in thick coal seam in Chenghe mining area of Weibei, China," *Environmental Earth Sciences*, vol. 79, no. 5, p. 118, 2020.

[16] T. Wei, G. Guo, H. Li, L. Wang, X. Yang, and Y. Wang, "Fusing minimal unit probability integration method and optimized quantum annealing for spatial location of coal goafs," *KSCE Journal of Civil Engineering*, vol. 26, no. 5, pp. 2381–2391, 2022.

[17] X. Xi, Z. Ding, R.-q. Ye, and R.-q. Niu, "Evaluation of geological environment carrying capacity of Huangshi city based on FCE-AHP," *Journal of Natural Resources*, vol. 36, no. 3, p. 646, 2021.

[18] X. Wang, J. Li, X. Zhao, and Y. Liang, "Propagation characteristics and prediction of blast-induced vibration on closely spaced rock tunnels," *Tunnelling and Underground Space Technology*, vol. 123, Article ID 104416, 2022.

[19] M. Gao, J. Xie, J. Guo, Y. Lu, Z. He, and C. Li, "Fractal evolution and connectivity characteristics of mining-induced crack networks in coal masses at different depths," *Geomechanics and Geophysics for Geo-Energy and Geo-Resources*, vol. 7, no. 1, p. 9, 2021.

[20] Y.-q. Su, F.-q. Gong, S. Luo, and Z.-x. Liu, "Experimental study on energy storage and dissipation characteristics of granite under two-dimensional compression with constant confining pressure," *Journal of Central South University*, vol. 28, no. 3, pp. 848–865, 2021.

[21] D. Chen, H. Chen, W. Zhang, J. Lou, and B. Shan, "An analytical solution of equivalent elastic modulus considering confining stress and its variables sensitivity analysis for fractured rock masses," *Journal of Rock Mechanics and Geotechnical Engineering*, vol. 14, no. 3, pp. 825–836, 2022.

[22] Q. Yin, J. Wu, Z. Jiang et al., "Investigating the effect of water quenching cycles on mechanical behaviors for granites after conventional triaxial compression," *Geomechanics and Geophysics for Geo-Energy and Geo-Resources*, vol. 8, no. 2, p. 77, 2022.

[23] Q. Wang, S. Xu, M. He, B. Jiang, H. Wei, and Y. Wang, "Dynamic mechanical characteristics and application of constant resistance energy-absorbing supporting material," *International Journal of Mining Science and Technology*, vol. 32, no. 3, pp. 447–458, 2022.

[24] P. Zhang, D. F. Zhang, Y. Yang et al., "A case study on intergrated modeling of spatial information of a complex geological body," *Lithosphere*, vol. 2022, Article ID 2918401, 2022.

[25] T. H. Tang, D. D. Sun, X. C. Xu, and X. Wang, "Problems and countermeasures in green, safe and efficient mining of large-scale open-pit mines in Xinjiang," *Journal of Mining & Safety Engineering*, vol. 39, no. 01, pp. 1–12, 2022.

[26] F. M. Li, X. P. Ding, G. L. Bai, and Z. Pan, "Eco-geological environment comprehensive management model of combined mining area of open-pit and underground mines in frigid plateau region," *Journal of China Coal Society*, vol. 46, no. 12, pp. 4033–4044, 2021.

[27] X. Y. Qu and X. L. Li, "The geological environment-related problems induced by underground coal mining and analysis of countermeasures," *Hydraulic Coal Mining & Pipeline Transportation*, vol. 03, pp. 129–131, 2019.

[28] H. H. Xu, W. L. Liu, L. Chen, S. G. Gui, F. Ding, and D. Liu, "Analysis on the characteristics of the karst collapse in Mudengdong Village of Gejiu Lao chang," *World Nonferrous Metals*, vol. 23, p. 274+276, 2017.

[29] H. H. Xu, W. L. Liu, Y. G. Hui et al., "Mechanism analysis of karst collapse in Laochang Town," *China Manganese Industry*, vol. 36, no. 02, pp. 62–65, 2018.

[30] M.-Z. Gao, B.-G. Yang, J. Xie et al., "The mechanism of microwave rock breaking and its potential application to rock-breaking technology in drilling," *Petroleum Science*, vol. 3, 2022.

[31] Z.-j. Wu, Z.-y. Wang, L.-f. Fan, L. Weng, and Q.-s. Liu, "Micro-failure process and failure mechanism of brittle rock under uniaxial compression using continuous real-time wave velocity measurement," *Journal of Central South University*, vol. 28, no. 2, pp. 556–571, 2021.

[32] Z. Dou, S. Tang, X. Zhang et al., "Influence of shear displacement on fluid flow and solute transport in a 3D rough fracture," *Lithosphere*, vol. 2021, no. Special 4, Article ID 1569736, 2021.

[33] Z. Dou, Y. Liu, X. Zhang et al., "Influence of layer transition zone on rainfall-induced instability of Multilayered slope," *Lithosphere*, vol. 2021, no. Special 4, Article ID 2277284, 2021.

[34] X. S. Li, Q. H. Li, Y. J. Hu et al., "Study on three-dimensional dynamic stability of open-pit high slope under blasting vibration [J]," *Lithosphere*, vol. 2022, Article ID 6426550, 2022.

[35] G. Li, Y. Hu, S.-m. Tian, M. weibin, and H.-l. Huang, "Analysis of deformation control mechanism of prestressed anchor on jointed soft rock in large cross-section tunnel," *Bulletin of Engineering Geology and the Environment*, vol. 80, no. 12, pp. 9089–9103, 2021.